Dalton
Transactions

PAPER

View Article Online
View Journal | View Issue

Cite this: *Dalton Trans.*, 2026, **55**, 1192

Triggering the intrinsic catalytic activity of electrodeposited CoNiFe LDH *via* Pt decoration for an efficient hydrogen evolution reaction

S. Vijaya and L. John Kennedy *

Received 9th July 2025,
Accepted 28th August 2025

DOI: 10.1039/d5dt01617g

rsc.li/dalton

Hydrogen is widely recognized as a clean and sustainable energy carrier, and the development of efficient, durable electrocatalysts for the hydrogen evolution reaction (HER) remains a key challenge in realizing large-scale hydrogen production. In this study, we report a two-step synthesis of a platinum decorated CoNiFe layered double hydroxide (Pt@CNF) electrocatalyst, engineered to enhance HER performance. Field-emission scanning electron microscopy (FE-SEM) confirms the uniform distribution of Pt nanoparticles on CoNiFe LDH (CNF) nanosheets. The incorporation of Pt, possessing an optimal hydrogen adsorption energy, significantly reduces the overpotential from 215 mV (CNF) to 117 mV (Pt@CNF) at a current density of 10 mA cm^{-2}. The enhanced intrinsic activity of Pt@CNF is further evidenced by a substantial increase in turnover frequency (TOF) from 7.1×10^{-3} s^{-1} to 14.6×10^{-3} s^{-1}. Additionally, Pt@CNF exhibits a larger electrochemical surface area (ECSA) and higher active ECSA (A_{ECSA}) compared to pristine CNF, reflecting the greater density of accessible catalytic sites. The synergy between Pt and the CNF matrix improves both charge transfer kinetics and catalytic durability, enabling Pt@CNF to deliver low overpotentials of 298, 370, and 441 mV at high current densities of 100, 200, and 400 mA cm^{-2}, respectively. These findings highlight the potential of Pt@CNF as a high-performance HER electrocatalyst for next-generation hydrogen production technologies.

Introduction

The escalating global energy demand, driven by industrial expansion and population growth, has underscored the urgent need for clean, efficient, and sustainable energy alternatives. In recent years, hydrogen based economy has experienced rapid growth in the field of energy due to hydrogen's highest gravimetric energy density with zero carbon content.[1–4] A green and sustainable method to produce hydrogen gas is through electrochemical water splitting, which utilizes renewable electricity to split water into hydrogen and oxygen without emitting greenhouse gases.[5] The electrochemical water splitting process proceeds *via* two half-cell reactions: the cathodic HER and anodic oxygen evolution reaction (OER). The generation of H^+ ions *via* the dissociation of water molecules in the HER process is slower under alkaline conditions than under acidic conditions. Therefore, a major challenge depends on developing efficient electrocatalysts that can accelerate both half-reactions: the hydrogen evolution reaction (HER) and the oxygen evolution reaction (OER) simultaneously.[6]

Often, carbon-supported noble-metal nanomaterials (such as Pt, Rh, Ru, and Ir) are extensively studied for the HER due to their near-ideal hydrogen binding energies, excellent stability, and tunable properties.[7,8] The carbon support not only provides a highly conductive matrix but also modifies the electronic structure of the noble metals through interfacial interactions, boosting catalytic performance.[9] The major challenge for carbon materials under alkaline conditions is corrosion of both the active catalyst phase and the support materials at high overpotentials at the anode. This degradation limits their thermodynamic instability under anodic conditions.[10] Furthermore, carbon can undergo oxidation to CO or CO_2 at potentials above 0.207 and 0.518 V *vs.* RHE. Although the kinetics of carbon corrosion are slow under typical operation, prolonged or accidental exposure to high potentials (>1.5 V *vs.* RHE) such as during start-up/shut-down cycles or fuel starvation events can trigger carbon degradation. This leads to loss of active metal species, agglomeration, and disruption of conductive pathways, ultimately compromising the durability and efficiency of the electrocatalytic system.[11] To address this limitation, layered double hydroxides (LDHs) have emerged as promising support materials, offering chemical stability, tunable composition, and strong metal–support interactions, thereby enhancing both the activity and longevity of electro-

---

Department of Physics, School of Advanced Sciences, Vellore Institute of Technology (VIT), Chennai, Tamil Nadu, India. E-mail: ljkennedy14@gmail.com

catalytic systems. In this regard, transition metal-based materials, especially layered double hydroxides (TM-LDHs), have gained attention due to their 2D structure, large surface area, tunable composition, and Earth abundance, making them strong candidates for both the HER and OER.[12] LDHs such as Ni–Co, Mn–Co, Co–Al, Ni–Mn, and especially NiFe based LDHs, have shown promising performance for overall water splitting.[3] Ni-based LDHs (*e.g.*, NiFe and NiCo) exhibit excellent OER activity in alkaline media due to their high surface area and compositional tunability. The engineering of strong metal support interactions (SMSI) has emerged as a powerful strategy to tailor the structural and catalytic properties of supported metal catalysts. SMSI can significantly influence the electronic structure, geometric configuration, and surface chemistry of metal nanoparticles, thereby enhancing their catalytic reactivity and stability. Furthermore, by tuning the composition of both the metal and support, SMSI can effectively prevent nanoparticle aggregation, improve metal dispersion, and increase the utilization efficiency of noble metals.[13] Moreover, noble metal doping (*e.g.*, Ru and Ir) can significantly enhance both the HER and OER by optimizing intermediate adsorption energies, though stability remains a concern. Importantly, the synergistic interactions between noble metals and LDHs are still underexplored, offering scope to improve activity and durability while minimizing noble metal usage.[6] LDHs, which are composed of metal hydroxide layers and intercalated anions, are known for their superior water dissociation properties. These materials support the cleavage of the H–OH bond, a crucial step in the electrolysis of water, and can efficiently adsorb and activate OH^- ions, improving the overall reaction kinetics in alkaline environments. When Pt is incorporated with LDHs, the resulting hybrid materials combine the excellent HER activity of Pt with the superior water dissociation and OH^- adsorption capabilities of the hydroxide component. Chen *et al.*[14] have developed NiFeRu LDH by substituting Ru into NiFe LDH to overcome the sluggish water dissociation kinetics of NiFe LDH. The NiFeRu LDH required only 1.52 V to reach the benchmark current density of 10 mA cm^{-2} in alkaline medium. In another study,[15] the sluggish water dissociation rate of NiFe LDH was significantly enhanced by doping with Ir^{4+} ions. Similarly, Pt (single atom) NiCo LDH exhibited faster electron transfer kinetics compared to NiCo LDH during the HER process. This improvement is attributed to the role of Pt as an H^+ ion capture center, facilitated by the formation of Pt–O bonds, which promote the efficient release of hydrogen gas.[16] Furthermore, density functional theory (DFT) of NiCo LDH reveals that its poor HER activity is due to the insufficient adsorption of hydrogen intermediates on its surface. However, the incorporation of Pt significantly increased the hydrogen intermediate adsorption energy, enabling stronger adsorption of these intermediates, thereby enhancing the HER performance.[16] The synergistic hybrid electrocatalyst MoS_2/NiCo LDH facilitated the chemisorption of hydrogen on MoS_2 and the hydroxyl intermediate on NiCo LDH at the heterointerface, thereby promoting the kinetics of the water dissociation process in an alkaline environment.[1] Additionally, the synergistic effect formed between Pt and NiFe LDH is beneficial for the overall performance of the HER process under alkaline conditions. The heterointerface formed between Pt and NiFe LDH not only improved the HER activity but also enhanced the electrochemical durability of the catalyst. This nanohybrid design resulted in plenty of exposed active sites, while the uniform Pt distribution over CoNiFe LDH effectively shortens the charge transfer path to deliver the best overall performance.[17]

The preparation of nanostructured LDHs is an effective approach to enhance water molecule dissociation by increasing the number of active sites. Compared to methods such as hydrothermal synthesis, corrosion engineering, and atomic layer deposition (ALD), electrodeposition offers a cost-effective, efficient, and binder-free approach suitable for practical applications.[18] In addition, structural transformations during electrochemical testing such as phase reconstruction or *in situ* activation often lead to enhanced activity. For instance, the electrochemical deposition performed using the cyclic voltammetry technique produced more active amorphous NiFe hydroxides.[19] This is because amorphous materials offer unique electrocatalytic properties due to their disordered atomic structure and absence of long-range periodicity. Also, the amorphous surface provides abundant defect sites and unsaturated coordination environments that stabilize the metal single atoms.[20] Furthermore, this technique enables the vertical growth of LDH nanosheet arrays, resulting in hierarchical nanostructures with a large surface area and abundant redox-active sites. Additionally, the porous structure formed through electrodeposition facilitates rapid ion diffusion, significantly boosting electrocatalytic performance. For example, electrodeposited NiFe LDH has been shown to possess an amorphous structure, as confirmed by the absence of characteristic XRD peaks.[21] The Pt/NiFe LDH prepared *via* electrodeposition exhibited a lower overpotential for the HER activity compared to Pt/NiFe synthesized through hydrothermal methods. Similarly, the direct electrodeposition of NiFeCo LDHs resulted in an amorphous, porous 2D orientation with excellent electrocatalytic activity for overall water splitting.[22] Notably, the direct growth of nanostructured electrocatalysts *via* electrodeposition enables high current densities with low overpotentials, attributed to their high surface area and optimized morphology.[23] This highlights the significant potential of electrodeposited LDHs for advancing electrolysis.

In this work, we present a strategy to construct an efficient hybrid electrocatalyst by incorporating Pt to enhance the HER activity of CoNiFe LDH (CNF) under alkaline conditions. A self-standing CNF was developed to eliminate the need for conducting carbon additives, which lack thermodynamic stability in alkaline media. LDHs prepared *via* direct growth offer inherent stability under such conditions, ensuring both durability and sufficient conductivity for efficient hydrogen evolution. The direct growth of amorphous CNF was achieved using a cost-effective electrodeposition method, while Pt incorporation was accomplished *via* a chemical reduction route.

The electrodeposited CNF exhibited an amorphous structure with highly exposed active sites, which are crucial for enhanced catalytic performance. The electrocatalytic activity of both CNF and Pt incorporated CoNiFe LDH (Pt@CNF) was evaluated for HER applications in 1 M KOH solution. Pt@CNF demonstrated a significantly lower overpotential value of 117 mV compared to CNF (215 mV) to attain a current density of 10 mA cm^{-2}. The incorporation of Pt introduced abundant active sites on the Pt@CNF surface, which substantially reduced the overpotential and enhanced HER performance. This is further evidenced by the high TOF of 14.6×10^{-3} s^{-1}, indicating improved intrinsic activity. Additionally, the Pt@CNF exhibited excellent durability in 1 M KOH, maintaining stable performance over time. To explore practical applicability, a symmetric device was fabricated, which required a low potential of 1.64 V to achieve the benchmark current density of 10 mA cm^{-2}. These results demonstrate that Pt incorporation effectively enhances the HER performance of CNF, highlighting an efficient strategy for developing self-supported hybrid nano-electrocatalysts with superior intrinsic catalytic activity for HER applications.

Experimental

Materials

Cobalt nitrate hexahydrate $Co(NO_3)_2{\cdot}6H_2O$, nickel nitrate hexahydrate $Ni(NO_3)_2{\cdot}6H_2O$, iron nitrate nonahydrate ($Fe(NO_3)_3{\cdot}9H_2O$), KOH, hexachloroplatinic acid $H_2PtCl_6{\cdot}6H_2O$, and $NaBH_4$ were procured from Merck. All the chemicals were used as received. Nickel foam (NF) was procured from Winfay Group Company Limited, Shanghai, China. A commercially available graphite rod was employed as a counter electrode in this work.

Synthesis of CoNiFe LDH on Ni foam

Herein, NF was used as a substrate for self-supporting catalysts because it facilitates rapid oxygen and electrolyte transport owing to its three-dimensional (3D), interconnected porous structure.[18] Firstly, bare NF (3×1 cm^2) was cleaned with ethanol in a water bath sonicator for 10 minutes and dried naturally. The direct growth of CNF was performed over NF (the working electrode) by directly applying −1.2 V for 50 s.[18,21,22] The electrolyte solution was prepared by dissolving 1 mM $Co(NO_3)_2{\cdot}6H_2O$, 2 mM $Ni(NO_3)_2{\cdot}6H_2O$, and 1 mM $Fe(NO_3)_3{\cdot}9H_2O$ in water. A commercial graphite rod served as a counter electrode and an Ag/AgCl electrode was employed as a reference electrode. After electrodeposition, the NF changed to light green color indicating the formation of CNF. The CNF coated NF was rinsed with water and ethanol to remove unreacted nitrate residues. Finally, the electrodes were dried at room temperature under ambient conditions. The weight of CNF on NF was found to be approximately 1.2 mg. The mass loading of CNF after electrodeposition was obtained by subtracting the weight of bare NF from the weight of CNF coated NF. The as-prepared CNF/NF was directly used for further characterization studies.

Synthesis of Pt@CoNiFe LDH

To synthesize the Pt@CNF electrode, 10 mg of hexachloroplatinic acid was dissolved in 1 mL of de-ionized water and coated directly over the electrodeposited CNF/NF to achieve uniform deposition. Then, this electrode was soaked in $NaBH_4$ solution to reduce the Pt in its Pt^{4+} to Pt^0. Once the bubbling effect was over, the electrode was taken from the solution and washed several times with water and ethanol. Finally, the electrode was dried naturally in air and used for further characterization studies.

Material characterization

The structural analysis of NF, CNF, and Pt@CNF was conducted through X-ray diffraction (XRD) using a Rigaku SmartLab diffractometer. The surface morphology and elemental mapping of the samples were studied using a Zeiss EVO 10 high-resolution scanning electron microscope (HR-SEM) with LaB_6 emission and a SUPRA 55 field emission scanning electron microscope (FE-SEM). These analyses revealed the microstructural features, surface texture, and distribution of elements within the electrode materials. The Smart EDX accessory integrated into the HR-SEM was utilized for the line profile to provide information about the elemental analysis and spatial distribution of Pt, Co, and Ni. The surface chemical composition and oxidation states of the elements in Pt@CNF were characterized using X-ray photoelectron spectroscopy (XPS) with a Physical Electronics system. This technique offered high-resolution insights into the chemical states of elements present on the surface, such as Pt's oxidation state and its interaction with CNF. The XPS analysis also helped confirm the successful deposition of Pt on the CNF surface. To further understand the microstructure of the Pt@CNF electrocatalyst, high-resolution transmission electron microscopy (HR-TEM) was utilized (JEOL, Japan).

Electrochemical characterization

The electrochemical studies were conducted using a ZIVELAB multichannel electrochemical workstation. Cyclic voltammetry (CV) and linear sweep voltammetry (LSV) measurements were carried out in a conventional three-electrode configuration. The electrodeposited CNF and Pt@CNF served as working electrodes, a graphite rod was used as a counter electrode, and an Ag/AgCl electrode acted as a reference electrode. All experiments were performed in a 1 M KOH electrolyte solution. Before conducting the electrochemical studies, nitrogen gas was purged through the electrolyte for 10 minutes to eliminate dissolved oxygen. The LSV data for the NF, CNF, and Pt@CNF electrodes were obtained at a scan rate of 2 mV s^{-1} both with 100% iR compensation and without iR compensation to assess the practical applicability of the electrodes. The potential *vs.* the reversible hydrogen electrode (RHE) was calculated using the Nernst equation ($E_{RHE} = E_{(Ag/AgCl)} + 0.059 \times pH + 0.1976$ V). The Tafel slope values were derived from the LSV data. The double-layer capacitance (C_{dl}) was determined from CV curves recorded at different scan rates in the non-faradaic region. To evaluate the long-term electrochemical stability of the electrodes, a chronopotentiometric study was conducted by applying a constant current density of -10 mA cm^{-2} for a continuous 10 h duration.

Results and discussion

The Pt@CNF hybrid electrode is prepared through a straightforward two-step process. In the first step, CNF is directly electrodeposited onto a conductive NF substrate, forming a uniform and adherent nanosheet-like structure with abundant active sites. In the second step, platinum nanoparticles are incorporated onto the CNF surface by chemical reduction of $H_2PtCl_6{\cdot}6H_2O$ using $NaBH_4$ as the reducing agent. This method ensures fine dispersion of Pt nanoparticles across the LDH matrix resulted in hybrid Pt@CNF, which can enhance the overall electrocatalytic activity. The schematic representation of the preparation process is illustrated in Fig. 1a. Fig. 1b presents the symmetric device fabricated using Pt@CNF for the real time electrochemical water splitting process.

The XRD patterns of CNF and Pt@CNF are presented in Fig. S1. The XRD of the bare NF is included for comparison purposes. The diffraction peaks observed at 44.4°, 51.8°, and 76.3° correspond to the (1 1 1), (2 0 0), and (2 2 0) planes of bare NF (JCPDS card no. 01-087-0712) for both CNF and Pt@CNF. The absence of additional diffraction peaks in the XRD patterns of both CNF and Pt@CNF indicates the poor crystalline/amorphous nature of the electrodeposited CNF. The absence of distinct Pt diffraction peaks in the XRD pattern of Pt@CNF is due to low loading of Pt on the surface and high dispersion or small particle size (possibly <5 nm), which reduces XRD detectability. In addition, the amorphous nature suggests a lack of long-range crystalline order, which is often advantageous for electrocatalytic applications. Amorphous materials typically exhibit a higher density of exposed active sites and enhanced surface areas compared to their crystalline counterparts, contributing to superior catalytic activity. The observed amorphous nature of electrodeposited CNF is consistent with previously reported literature studies on electrodeposited LDHs,[22] which also highlight the benefits of amorphous structures in improving catalytic performance. The absence of sharp, well-defined peaks in the XRD patterns further supports the successful synthesis of amorphous CNF and Pt@CNF, aligning with the intended design strategy for enhancing electrocatalytic HER performance.

The XRD patterns of all samples deposited on NF predominantly exhibited the characteristic peaks of NF, indicating that the underlying substrate remains the major crystalline phase. However, variations in peak intensity were observed. In the case of the CoNiFe-LDH-coated sample, the diffraction peaks appeared broader and of lower intensity compared to bare NF, suggesting the formation of smaller crystallites and a more amorphous structure.[24] Upon Pt doping, a slight increase in peak intensity was noted relative to the undoped CoNiFe-LDH, although still lower than bare NF. This trend indicates that Pt incorporation enhances the crystallinity of the LDH layer, likely due to the formation of crystalline Pt domains or improved structural ordering within the LDH matrix.

The FE-SEM technique is employed to analyze the morphology of the CNF and Pt@CNF samples and the corresponding images are presented in Fig. 2. The CNF sample (Fig. 2a and b) exhibits nanosheet morphology (having the thickness of around 11–13 nm, Fig. S2a), which is beneficial

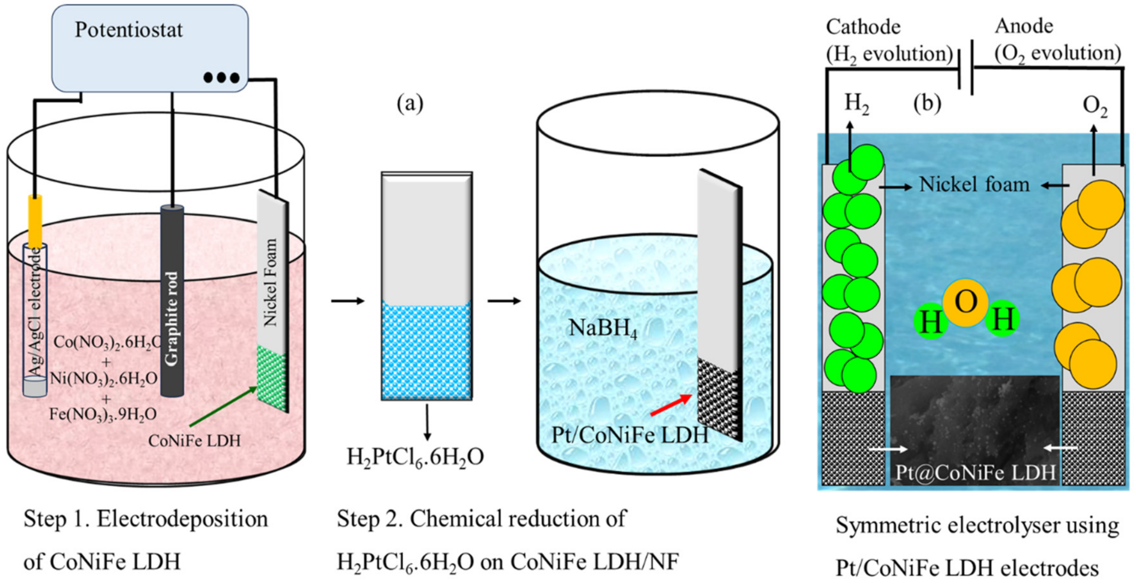

Fig. 1 Schematic representation of (a) the preparation of CNF and Pt@CNF, and (b) a symmetric electrolyser using two identical hybrid Pt@CNF electrodes.

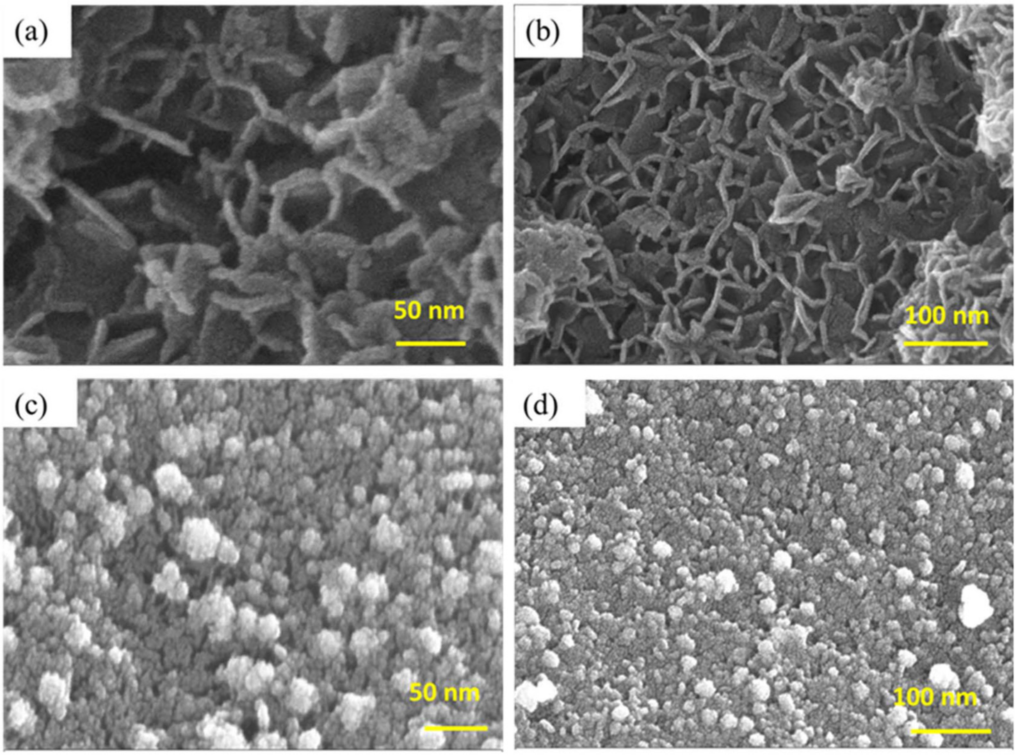

Fig. 2 FE-SEM images of (a and b) CNF and (c and d) Pt@CNF.

for catalytic applications. In the FE-SEM image of Pt@CNF (Fig. 2c and d), the Pt nanoparticles having various sizes (for instance, 4.2 and 4.6 nm, as shown in Fig. S2b) are highly dispersed over the CNF nanosheet surface. This uniform distribution of Pt nanoparticles is critical, as Pt plays a key role in catalyzing alkaline water splitting to efficiently generate hydrogen molecules. This demonstrates the successful incorporation of Pt into the CNF structure without disrupting its overall morphology. Furthermore, the SEM images reveal a uniform coating of the LDHs on the NF substrate, ensuring a stable and conductive support for the electrocatalyst.

EDX analysis is carried out to confirm the presence of Co, Ni, Fe, O, and Pt elements in the sample and to verify the elemental composition of the samples. The elemental analysis of CNF shown in Fig. 3a confirms the presence of Co, Ni, Fe, and O elements in the sample. The detection of Pt, even at low loading, along with the retained presence of Co and Fe, supports the formation of a Pt-modified CNF LDH (Fig. 3b). Additional HR-SEM line scanning profile analysis of both CNF and Pt@CNF, confirming the presence of Co, Ni, Fe, and Pt elements within the LDHs, is shown in Fig. S3a and b. These changes indicate SMSI between Pt and the CNF LDH matrix, which can enhance the electronic structure and catalytic performance for the alkaline HER. The weight% of Pt in Pt@CNF is found to be 0.8.

To further investigate the distribution of elements present in the sample, an elemental mapping study is conducted, and the results are exhibited in Fig. 4. The elemental maps show a homogeneous distribution of Co, Ni, and Fe in CNF (Fig. 4a–d) and Pt along with Co, Ni, and Fe in Pt@CNF (Fig. 4e–i) across the LDH surface, indicating effective mixing of the metal components and uniform dispersion of Pt. This uniformity enhances the catalytic activity by ensuring that all active sites are readily accessible and contribute to the overall HER performance. These findings highlight the synergistic effect of the nanosheet-like CNF structure and the Pt nanoparticles, which together provide an optimized platform for a high performance alkaline water splitting process.

To further understand the microstructure of the Pt@CNF electrocatalyst, HR-TEM has been performed. TEM analysis of the Pt@CoNiFe-LDH sample (Fig. 5a–c) reveals a nanosheet-like morphology, consistent with the features observed in FE-SEM images. High-resolution TEM further confirms the uniform distribution of Pt nanoparticles over the CoNiFe-LDH surface. The corresponding SAED pattern (Fig. 5d) exhibited diffuse rings, indicative of a non-crystalline nature. These observations are in agreement with the XRD results, which showed only the diffraction peak of the Ni foam substrate, with no distinct reflections attributable to Pt or CoNiFe-LDH.

XPS analysis is performed for the CNF and Pt@CNF catalysts to provide detailed insights into their chemical composition and the oxidation states of the elements such as Co, Ni, Fe, O, and Pt. The survey spectrum (Fig. 6a) confirms the presence of Co, Ni, Fe, O, and Pt elements on the surface of the catalyst. The high resolution spectra of Co, Ni, Fe, and O elements in Pt@CNF are compared with the undoped sample and are shown in Fig. 6b–i. The Co 2p spectrum reveals two primary peaks forming a doublet at

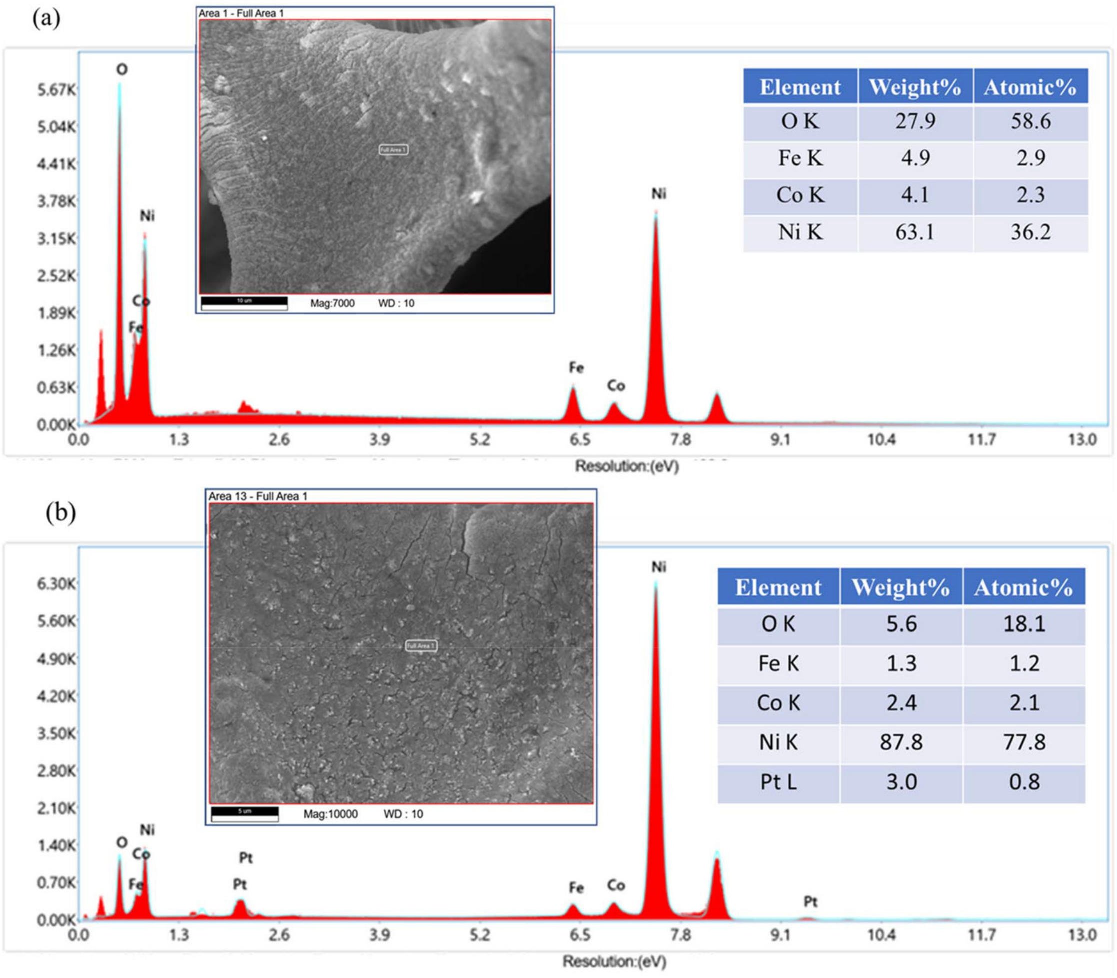

(a)

Element	Weight%	Atomic%
O K	27.9	58.6
Fe K	4.9	2.9
Co K	4.1	2.3
Ni K	63.1	36.2

(b)

Element	Weight%	Atomic%
O K	5.6	18.1
Fe K	1.3	1.2
Co K	2.4	2.1
Ni K	87.8	77.8
Pt L	3.0	0.8

Fig. 3 EDX analysis of (a) CNF and (b) Pt@CNF.

binding energies of 780.9 eV and 797.2 eV ascribed to the spin orbit splitting of $2p_{3/2}$ and $2p_{1/2}$, respectively. These peaks are further deconvoluted into four peaks, in which the peak located at 797.2 eV represents the presence of Co^{3+} and the existence of Co^{2+} can be identified at the binding energy of 780.9 eV along with two satellite peaks positioned at 786.7 and 803.2 eV, respectively. The presence of Co in its +2 oxidation state confirms the successful formation of $Co(OH)_2$ in CNF.[25–28] The high-resolution Co 2p XPS spectrum of the Pt@CNF sample exhibits a noticeable negative shift in the binding energy of Co^{2+} species and a positive shift for Co^{3+} species compared to pristine CNF, indicating strong electronic interactions of Pt in CNF. This shift reflects a strong electronic interaction between Pt and the CNF LDH support, confirming the presence of strong metal–support interactions (SMSI) in the Pt/CNF LDH system. It is worth noting that the modulation of SMSI is a powerful strategy for tuning the structure and performance of supported metal catalysts since it can influence the electronic structure, morphology, and composition of metal nanoparticles, thereby enhancing their catalytic activity and stability. Moreover, the conversion of Co from its Co^{3+} state to Co^{2+} state is possible because of the strong reducing agent $NaBH_4$ used for the deposition of Pt over CNF.[13,28] The high resolution Ni 2p spectrum shows the characteristic binding energy values of Ni in its +2 oxidation states at 855.6 and 873.2 eV. Along with these characteristic peaks, two prominent satellite peaks with the binding energy values of 861.6 and 879.8 eV are also observed, strongly suggesting the presence of $Ni(OH)_2$ in CNF. No significant changes of the Ni 2p peak shifting are observed after the introduction of Pt in CNF.[29] The high resolution Fe spectrum exhibits a spin orbit doublet at 712.1 eV (Fe $2p_{3/2}$) and 724.3 eV (Fe $2p_{1/2}$) corresponding to the +3 oxidation state of Fe. This further confirms the formation of $Fe(OH)_3$ in CNF. Two shake-up peaks located at 720.2 and 733.1 eV are also found in the Fe 2p spectrum.[29,30] The introduction of Pt influences the electronic configuration of Fe in Pt@CNF and, due to this, the high resolution XPS of Fe 2p in Pt@CNF shows a positive shift of Fe $2p_{3/2}$ and Fe $2p_{1/2}$ by 0.7 and 1.7 eV, respectively. This drastic change in electronic environment because of the Pt introduction can highly influence the HER performance and it is in good accord with the previous literature.[18,31] Additionally, the presence of iron in its +3 oxidation state within iron hydroxide $Fe(OH)_3$ is well supported by XPS analysis. In the Pt 4f spectrum shown in Fig. 6j, the doublet

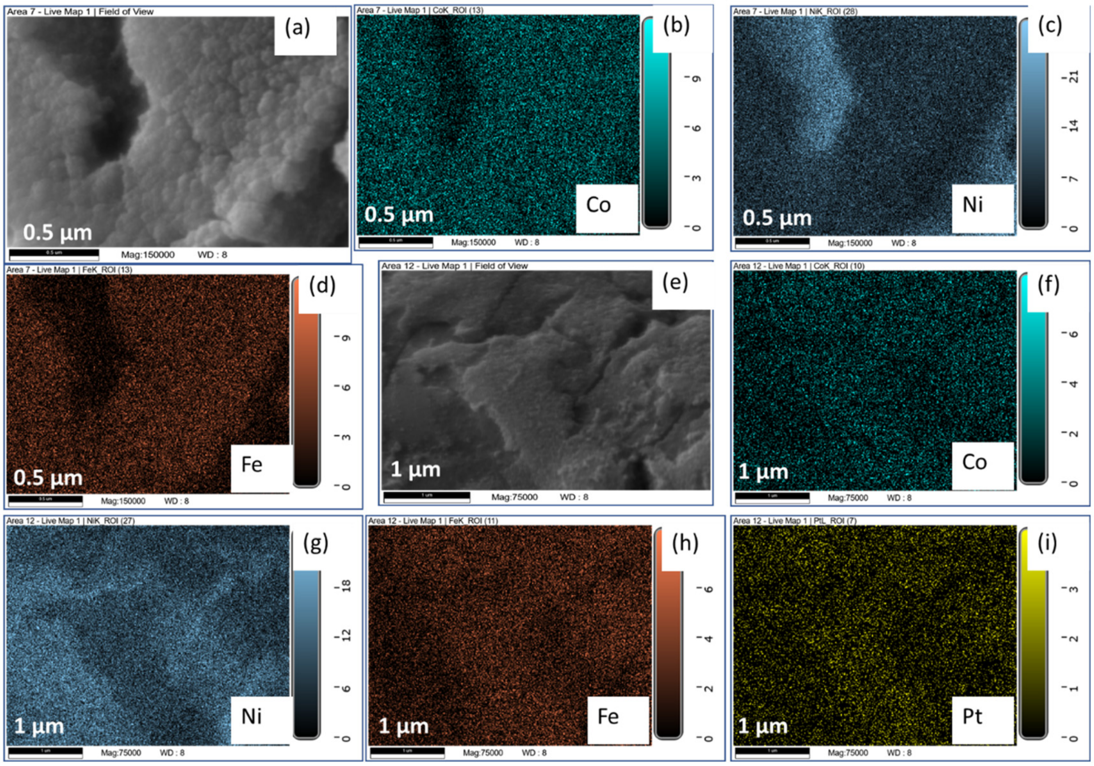

Fig. 4 HR-SEM images with elemental mapping of (a–d) CNF and (e–i) Pt@CNF.

at binding energies of 71.1 (Pt $4f_{5/2}$) and 74.2 eV (Pt $4f_{3/2}$) is consistent with metallic platinum (Pt^0), confirming the presence of metallic Pt on the catalyst surface.[18] Furthermore, the presence of Pt at its zero oxidation state confirms the complete reduction of Pt^{4+} by $NaBH_4$. The Pt in its zero oxidation state is important for its catalytic activity toward the HER. The O 1s spectrum provides additional evidence for the hydroxide formation on the catalyst surface. The peak at 533 eV corresponds to surface-adsorbed water molecules. The presence of chemisorbed hydroxyl groups (M–OH, where M represents the metal ions Co, Ni or Fe) is evidenced by the distinct binding energy at 531.3 eV, which is often involved in catalytic processes. The peak located at 529.6 eV confirms the presence of oxygen atoms bound directly to the metals (Co, Ni and Fe) in the hydroxide phase, confirming the presence of $Co(OH)_2$, $Ni(OH)_2$ and $Fe(OH)_3$ on the catalyst surface. Overall, the XPS analysis confirms the composition of the catalyst, which includes $Co(OH)_2$, $Ni(OH)_2$, $Fe(OH)_3$, and Pt metal. This detailed elemental and bonding information is crucial for understanding the surface chemistry of the catalyst and its potential catalytic activity. The presence of hydroxide species, in particular, suggests that the catalyst might have beneficial properties for reactions involving metal–oxide interfaces or the activation of water molecules. Also, the co-existence of Ni, Fe, and Co likely modulates the electronic structure, facilitating π-donation across the metal–oxygen bridges and promoting more efficient O_2 adsorption/desorption dynamics.[32–34] This also confirms the successful formation of CNF and the successful incorporation of Pt in CNF.

The HER performance of CNF and Pt@CNF was systematically evaluated using a standard three-electrode setup, which is a standard method for electrochemical measurements. In this setup, the CNF was grown on NF in which NF was used as the working electrode, with a graphite rod serving as the counter electrode and an Ag/AgCl reference electrode. Additionally, the electrocatalytic performance of bare NF was also evaluated under the same experimental conditions for comparison. The polarization plots for CNF and Pt@CNF are 100% *iR*-corrected (fully compensated for the ohmic resistance), as recommended in the literature[35] for accurate evaluation of electrocatalytic performance. The corrected polarization curves are shown in Fig. 7. For comparison, the polarization curve of bare NF is also included. From the polarization curves shown in Fig. 7a, it is evident that Pt@CNF exhibits a significantly lower overpotential compared to both CNF and bare NF when reaching the benchmark current density of 10 mA cm^{-2}. Specifically, Pt@CNF requires only 117 mV *vs.* RHE to achieve this target current density, whereas CNF and bare NF require 215 mV and 220 mV *vs.* RHE, respectively, to reach the same current density. Notably, Pt@CNF consistently shows the lowest overpotential when reaching higher current densities of 100, 200, and 400 mA cm^{-2} compared to both bare NF and CNF. Pt, despite its renowned catalytic properties, is often limited under alkaline conditions due to slow water dissociation and weak OH^- adsorption, which can hinder its overall catalytic efficiency. However, incorporating Pt into CNF successfully mitigates these limitations. The strong synergistic interactions between

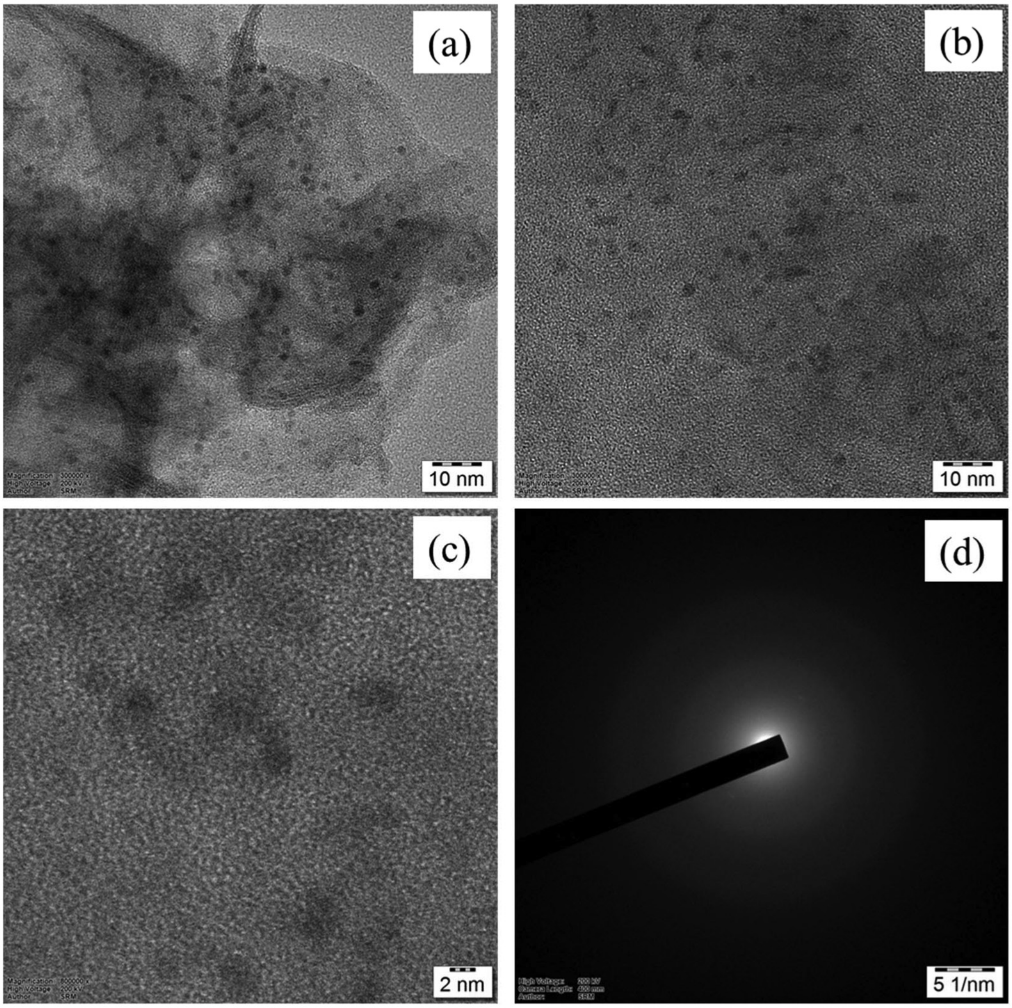

Fig. 5 (a–c) HR-TEM images and (d) SAED pattern of Pt@CNF.

Pt and CNF significantly enhance the overall HER performance.[17] This enhancement aligns with Sabatier's principle, which emphasizes that the bond strength between the metal (M) and the hydrogen atom (M–H) should be optimal for efficient hydrogen evolution. Therefore, hydrogen binding energy is an activity marker for the generation of the hydrogen molecule. After water dissociation during the Volmer step, an ideal M–H bond ensures that hydrogen molecules can be easily released, promoting high catalytic efficiency. Pt, with its near-optimal hydrogen binding energy, excels in facilitating this process.[36] Consequently, the Pt@CNF catalyst achieves a much lower overpotential compared to both pure CNF and bare NF, demonstrating superior HER activity. This performance improvement highlights the pivotal role of Pt incorporation and its synergistic effects with CNF in overcoming the intrinsic limitations of Pt in alkaline media, thereby unlocking its full potential as an electrocatalyst for hydrogen evolution. The HER activity performance of metal doped LDHs prepared *via* various methods is compared in Table 1.

For practical applications, the real water splitting process cannot operate at the overpotential obtained from the *iR* corrected polarization plot, and therefore, the uncompensated polarization plot is also required to test the possible applicability of the catalyst.[23] The recorded plots are shown in Fig. S4. The overpotential achieved for the CNF catalyst for the HER process is 238 mV and Pt@CNF shows an overpotential of 122 mV. The overpotential values observed with and without *iR* compensation are not the same, but it is expected and still meaningful. This highlights the additional energy requirements caused by resistive losses in the electrochemical system, which must be accounted for during the practical operation of water-splitting devices. The results emphasize the importance of evaluating both *iR* corrected and uncompensated data to provide a realistic assessment of the catalyst's performance, bridging the gap between ideal laboratory conditions and practical applications.

The Tafel study is an important activity metric for the investigation of the reaction pathways followed by electrocatalysts employed in water splitting. The electrochemical reactions

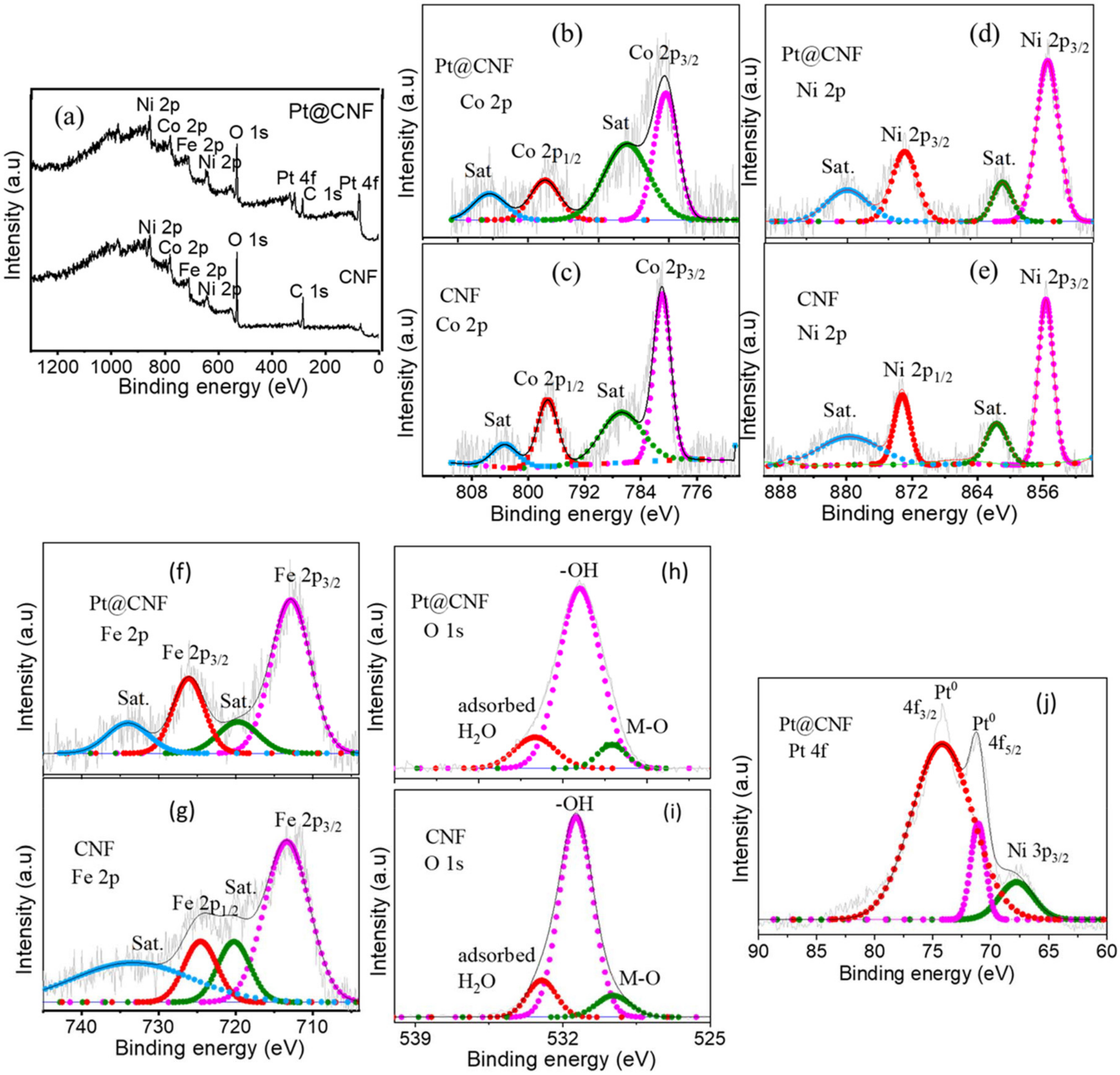

Fig. 6 XPS of CNF and Pt@CNF. (a) Survey spectra; (b–i) high resolution spectrum of Co 2p, Ni 2p, Fe 2p, and O 1s; and (j) high resolution spectra of Pt 4f.

(eqn (1)–(3)) involved in the HER process under alkaline conditions are given as[41]

$$H_2O + e^- + M \rightarrow M\text{–}H + OH^- \ \text{(Volmer)} \tag{1}$$

$$H_2O + e^- + M\text{–}H \rightarrow H_2 + OH^- \ \text{(Heyrovsky)} \tag{2}$$

$$2M\text{–}H \rightarrow 2M + H_2 \ \text{(Tafel)} \tag{3}$$

where M represents the vacant site and M–H represents the adsorbed hydrogen atom (H_{ads}). The formation of M–H intermediates, essential for hydrogen evolution, begins with the dissociation of water molecules, making the Tafel slope an indicative parameter of the catalytic efficiency and reaction mechanism. Among these, the Volmer reaction is often the rate determining step (RDS), primarily due to the sluggish kinetics of water dissociation in which high activation energy is required to break the O–H bond in water. This makes the Volmer step inherently slow in alkaline electrolytes, thereby controlling the overall HER kinetics. From the polarization plots (Fig. 7b), the Tafel slope for the Pt@CNF catalyst is calculated to be 137 mV dec^{-1}, which is slightly higher than that of CNF (125 mV dec^{-1}) but significantly lower than that of the bare NF, which exhibits a Tafel slope of 171 mV dec^{-1}. Even though Pt is excellent at hydrogen adsorption and desorption, under alkaline conditions, the Volmer step, where water is split into adsorbed hydrogen (H) and hydroxide (OH^-), becomes the RDS due to its high energy barrier. This results in Tafel slopes that are significantly higher than those observed in acidic environments, indicating sluggish water dissociation. As reported in the literature,[23] the Tafel slope in alkaline media is inherently higher for Pt-based catalysts because of this extra energy requirement. Evidently, DFT and kinetic

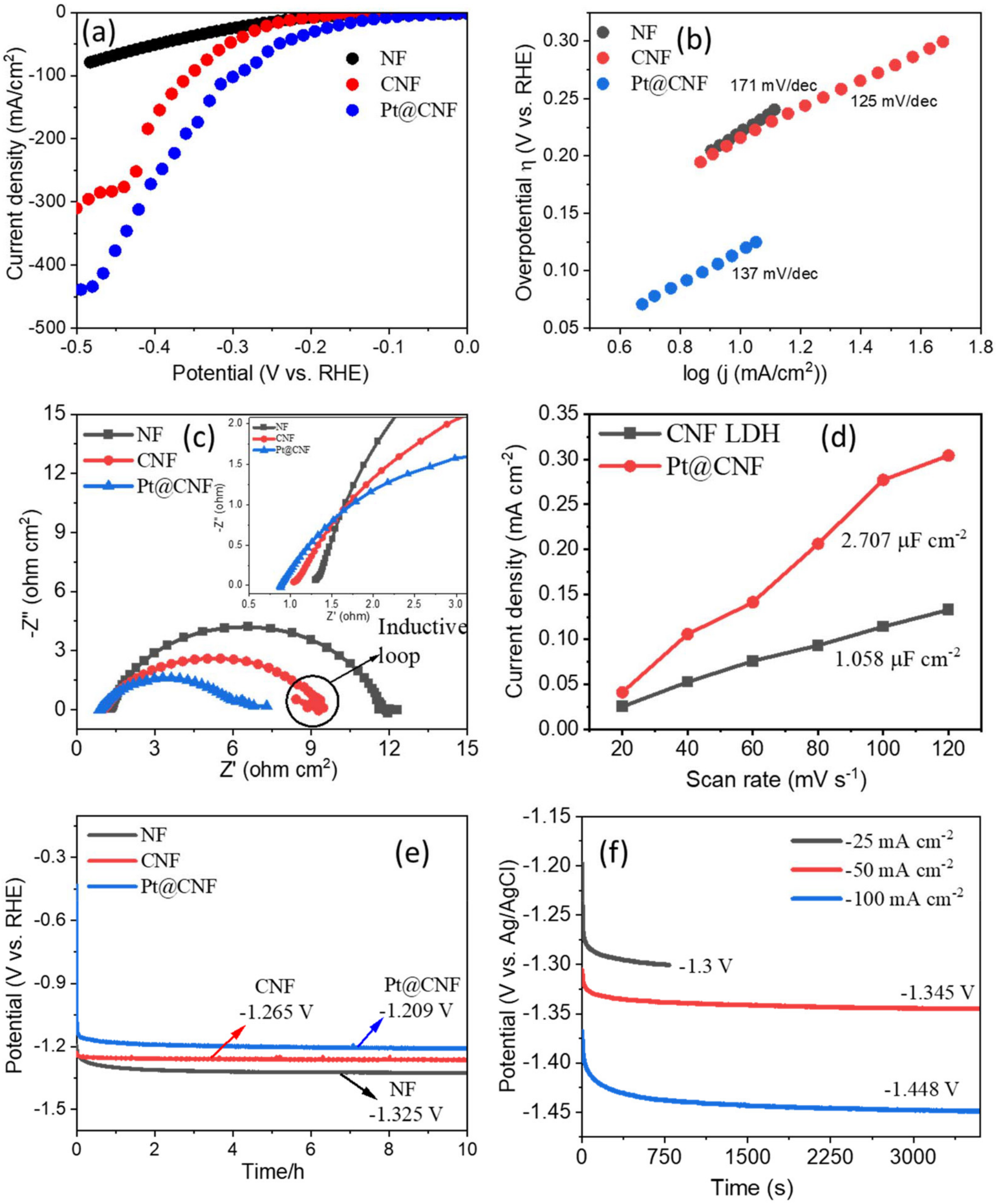

Fig. 7 (a) LSV polarization plots; (b) Tafel slopes; (c) Nyquist plots of NF, CNF, and Pt@CNF; (d) capacitive current density as a function of scan rate of CNF and Pt@CNF; (e) chronopotentiometry of NF, CNF, and Pt@CNF; and (f) chronopotentiometry of Pt@CNF at different current densities.

Table 1 Comparison of the HER activity of metal doped LDHs prepared *via* various methods

Sample	Method	η_{10} (mV)	Tafel slope (mV dec^{-1})	Ref.
V–NiFe-LDH/NF	*In situ* growth *via* a simple surface redox etching	120	89.8	37
Ce-doped NiFe-LDH	Electrodeposition	147	112	3
$Co_{1-x}Fe_x$-LDH	Direct growth-hydrothermal	242	98	38
$Ni_{1-x}Fe_x$-LDH	Direct growth-hydrothermal	205	110	38
Pd^{2+} doped NiFe LDH	Hydrothermal	316	135.8	39
Pt NPs tethered NiFe LDH	Hydrothermal	101	127	40
Pt@CNF	Electrodeposition followed by chemical reduction	117	137	This work

studies show that the energy barrier for splitting H_2O on Pt in alkaline electrolytes is typically 0.9–1.0 eV, which is considerably high and slows down the Volmer step.[42] Furthermore, Pt in its metallic Pt^0 state with its fully filled e_g orbitals exhibits weak binding affinity toward H_2O molecules. As a result, Pt^0 primarily serves as an active site for H_2 evolution and desorption rather than for water adsorption or activation. In contrast, Fe^{3+} species, characterized by half-filled e_g orbitals, form moderately strong bonds with oxygen-containing intermediates. This electronic configuration is advantageous for facilitating H_2O adsorption and activation, which is essential in the Volmer step of the HER in alkaline media.[43] Therefore, Pt exhibits improved alkaline HER performance when paired with oxophilic promoters like $Ni(OH)_2$. These co-catalysts facilitate water dissociation, while Pt handles hydrogen adsorption/recombination. Without such promoters, Pt alone struggles, reinforcing that Pt's inherent water dissociation kinetics is poor in alkaline media.[44] Therefore, the higher Tafel slope for Pt@CNF compared to CNF suggests that Pt incorporation modifies the reaction pathway while still enhancing HER performance relative to bare NF. The difference in Tafel slope values reflects the intrinsic reaction kinetics of the catalysts under alkaline conditions.

The HER kinetics of bare NF, CNF and Pt@CNF is further examined using electrochemical impedance spectroscopy (EIS). The Nyquist plots of bare NF, CNF, and 7Pt@CNF electrodes are presented in Fig. 7c. The inset shows that the solution or electrolyte resistance (R_s) is lowest for Pt@CNF compared to CNF and bare NF. This is attributed to the enhanced electrical conductivity of Pt@CNF, which facilitates improved charge transfer during the HER process, as supported by the literature.[6,41] The trend in solution resistance follows the order Pt@CNF < CNF < NF, highlighting the superior conductivity of the Pt incorporated electrode. Interestingly, the Nyquist plot for the pure CNF electrode exhibits an inductive loop behavior, whereas no such behavior is observed for Pt@CNF or bare NF. The presence of the inductive loop in CNF suggests that this electrode follows the Heyrovsky reaction pathway during the HER process, which involves both the adsorption and electrochemical desorption of hydrogen intermediates. This behavior aligns with the slightly lower Tafel slope value observed for CNF compared to Pt@CNF, indicating different kinetic mechanisms between the two electrodes.[45] The inductive loop in the Nyquist plot serves as a key indicator of the reaction pathway involved in the HER mechanism. Overall, the Nyquist plot analysis complements the Tafel slope findings, providing consistent evidence for the HER kinetics and the underlying reaction mechanisms of the tested electrodes.

To accurately assess the intrinsic activity of a catalyst, parameters such as turnover frequency (TOF) and electrochemically active surface area (ECSA) are considered reliable intrinsic activity markers, as they remain independent of the mass loading of the electrocatalyst.[35] Among these, ECSA is particularly relevant because it directly correlates the number of active sites to the real surface area of the catalyst, providing valuable insights into its intrinsic catalytic activity. To evaluate the intrinsic activity of CNF and Pt@CNF, ECSA was determined using CV in the non-faradaic region (Fig. S5), where the current response is governed by the double-layer capacitance (C_{dl}). The C_{dl} values can be derived from the slope of the linear fitting of current density *versus* scan rate plots, as shown in Fig. 7d. The calculated C_{dl} value for Pt@CNF was found to be 2.707 μF cm^{-2}, significantly higher than that of the CNF electrode (1.058 μF cm^{-2}), indicating a larger number of exposed active sites in Pt@CNF. In addition to this, the active electrochemical surface area (A_{ECSA}) represents the effective surface area of the catalyst that actively participates in the electrochemical reaction. A_{ECSA} is derived by normalizing the C_{dl} values to the specific capacitance (C_s) of a flat surface, which allows for a direct comparison of the number of exposed active sites between catalysts. Hence, from the C_{dl} values obtained, the A_{ECSA} was further calculated by following eqn (4)[46,47]

$$A_{ECSA} = \frac{C_{dl}}{C_s} \tag{4}$$

where C_{dl} represents the double layer capacitance and C_s represents the specific capacitance. The specific capacitance (C_s) value for a smooth standard with a real surface area of 1 × 1 cm^2 is taken as 40 μF cm^{-2} from the literature.[46] For the Pt@CNF electrode, the A_{ECSA} is calculated as 0.067 cm^2, which is significantly higher than that of the pure CNF electrode (0.026 cm^2). This larger A_{ECSA} value for Pt@CNF indicates that the incorporation of Pt has enhanced the surface's electrochemical activity by increasing the number of accessible active sites. This increase is attributed to the synergistic effect between Pt and the CNF, where Pt not only contributes its own catalytic activity but also modifies the electronic structure of the LDH, exposing more active sites and enhancing charge transfer efficiency. Thus, the higher A_{ECSA} values for the Pt incorporated electrodes (both Pt@CNF and Pt@CNF) reflect their superior intrinsic catalytic activity, making them more efficient for the electrochemical HER. This demonstrates the importance of Pt incorporation in improving the electrochemical performance of composite materials. The continuous generation of hydrogen gas for a 10 h duration is conducted to test the durability of the electrodes. The chronopotentiometry of the corresponding electrodes are shown in Fig. 7e. The Pt@CNF requires only 1.209 V to achieve the benchmark current density of 10 mA cm^{-2} which is lower than CNF (1.265 V) and much lower than the pure NF (1.325 V). The overpotential values obtained from the LSV plot show the catalyst's potential of reaching higher current densities, even more than −400 mA cm^{-2}. To further validate the catalytic performance of Pt@CNF, chronopotentiometry at high current densities like −25, −50, and −100 mA cm^{-2} is conducted, and the plots of the same are shown in Fig. 7f. Previous studies have shown that Pt modification of LDHs significantly enhances HER performance by accelerating reaction kinetics. Expanding on this, Yang *et al.*[48] provided new insights into the water electrolysis mechanism in transition metal hydroxides by developing a thulium (Tm) incorporated and Pt modified Ni_3Fe LDH to enhance HER activity. The resulting catalyst Ni_3Fe LDH/

$NiFe_2O_4$/Pt–Tm showed a low overpotential of 125 mV to reach a current density of 10 mA cm^{-2}. With these electrodes, overall water splitting was achieved at 1.69 V in 1.0 M KOH, demonstrating excellent bifunctional catalytic efficiency.

Turnover frequency (TOF) is a crucial metric used to assess the intrinsic activity of an electrocatalyst. Intrinsic activity is a fundamental parameter that reflects the inherent ability of the catalyst to drive the HER at its active sites. Consequently, TOF is widely regarded as an intrinsic activity marker, offering a more precise evaluation of the HER performance of a catalyst compared to metrics based solely on the electrode surface area.[21] TOF is particularly significant because it provides direct insights into the rate of hydrogen molecule evolution, a key parameter for understanding the efficiency of HER catalysts.[23] For the current study, the TOF values of CNF and Pt@CNF electrodes were calculated using the formula given in the previous studies.[49,50] The TOF for Pt@CNF is found to be 14.6×10^{-3} s^{-1}, which is approximately two times higher than that of pure CNF, whose TOF is 7.1×10^{-3} s^{-1}. This substantial improvement in TOF for Pt@CNF confirms the presence of a greater number of active catalytic sites compared to CNF. These findings strongly suggest that the superior HER performance of Pt@CNF originates from the high density of active sites within the catalyst, enabling efficient redox reactions.[51] It is noteworthy that the TOF values can vary depending on the structural and chemical heterogeneity of active sites within the catalyst. Hence, quantifying TOF is more informative than relying solely on surface area measurements, as TOF provides a clearer picture of the activity at each site.[52]

In the context of alkaline HER, the theoretical hydrogen gas yield serves as an important indicator of the electrocatalyst's efficiency in driving hydrogen evolution. By assuming 100% faradaic efficiency, the amount of hydrogen evolved corresponds directly to the current passed during the reaction, providing insights into the effectiveness of the catalyst under the applied overpotential.[46] At an overpotential of 183 mV, the Pt@CNF catalyst achieves a theoretical hydrogen yield of 7.7 μmol, significantly surpassing the yield of 0.5 μmol obtained for the pure CNF electrode under the same conditions. This remarkable difference highlights the enhanced catalytic activity of Pt@CNF in the alkaline HER process.

High current densities are typically required for industrial-scale hydrogen production. Therefore, it is essential for electrodes to perform efficiently not only under laboratory conditions where 10 mA cm^{-2} is often used as a benchmark but also under commercial-scale operating conditions involving much higher current densities. The Pt@CNF electrode demonstrates excellent performance by achieving a current density of 400 mA cm^{-2}, highlighting its strong potential for practical, large-scale hydrogen production. The plots of overpotential comparison of NF, CNF and Pt@CNF at the overpotentials of 10, 100, 200, and 400 mA cm^{-2} is shown in Fig. 8a. The practical applicability of the Pt@CNF at 50 mA cm^{-2} is tested for 60 seconds by constructing a symmetric device. The device requires only 1.942 V to reach the high current density of 50 mA cm^{-2} at the end of 60 seconds (Fig. 8b). The two-electrode approach is a straightforward, cost-effective, and practical method to study water splitting. To validate the practical applicability of the constructed Pt@CNF electrodes, two electrode configuration of Pt@CNF||Pt@CNF is fabricated and tested for 10 h of continuous hydrogen generation for real time applications. The symmetric device requires only 1.63 V to achieve a current density of 10 mA cm^{-2} (Fig. 8c), which is notably better compared to the previously reported Ni_3Fe LDH/$NiFe_2O_4$/Pt–Tm electrodes, which required 1.69 V for overall water splitting in 1 M KOH.[48]

Post-HER analysis

To elucidate the possible chemical composition and oxidation states of Co, Ni, Fe, and Pt during HER activity in the Pt@CNF electrode, the XPS technique is employed. The change in chemical composition and oxidation states of the elements present in Pt@CNF after 10 h stability is investigated by the XPS technique. The survey spectrum (Fig. S6a) of the post stability study of the Pt@CNF electrode indicates the elemental presence of Fe, Co, Ni, C, Pt, and O species. The high resolution Co 2p spectrum (Fig. S6b) indicates the presence of Co majorly in its higher oxidation states (Co^{2+}) compared to Co^{3+}. The existence of Co^{3+} active species in the form of CoOOH is evidenced by the high resolution spectra of Co 2p after the HER stability test.[53,54] The post-HER high resolution spectrum of Ni 2p (Fig. S6c) corresponding to Ni^{3+} shows a negative peak shift by 0.3 eV. The signal corresponding to Co^{3+} species moves to a lower binding energy by 1 eV and the signal corresponding to Fe^{3+} species moves to a higher binding energy by 0.3 eV (Fig. S6d). In addition, a lower binding energy shift by 0.2 eV is observed for Pt^0 (Fig. S6e). All these changes indicate a certain degree of surface reconstruction in Pt@CNF during the HER process and it is consistent with the previous literature.[43] The peak at 532.6 eV is attributed to the adsorbed oxygen species, specifically from hydroxyl groups such as adsorbed H_2O molecules (Fig. S6f).[55] The high resolution spectra of O 1s confirm the increased adsorbed water molecule at the hybrid Pt@CNF electrode after the post stability study. The adsorbed water molecule at the electrode surface during the HER in aqueous KOH electrolyte is confirmed by the signal at 532.6 eV in high resolution spectra of O 1s.[28] The presence of the K element is also evidenced by the high resolution spectra of K 2p in the XPS analysis.

The electrodes after 10 h of continuous HER are investigated by HR-SEM studies and the images are shown in Fig. S7. Post-HER HR-SEM images reveal significant structural degradation in the undoped CNF LDH electrode, including clear signs of surface peeling and delamination from the nickel foam substrate. This suggests poor mechanical stability under alkaline electrochemical conditions. In contrast, the Pt@CNF LDH electrode maintains a more intact and adherent morphology, with minimal peeling observed. This enhanced interfacial adhesion can be attributed to the stronger electronic and structural interactions between Pt species and the LDH framework, which likely reinforce the anchoring of the active layer to the substrate and mitigate delamination during prolonged HER operation. EDX analysis of Pt@CNF (Fig. S8) reveals that the atomic percentage of Pt (0.5%) remains largely

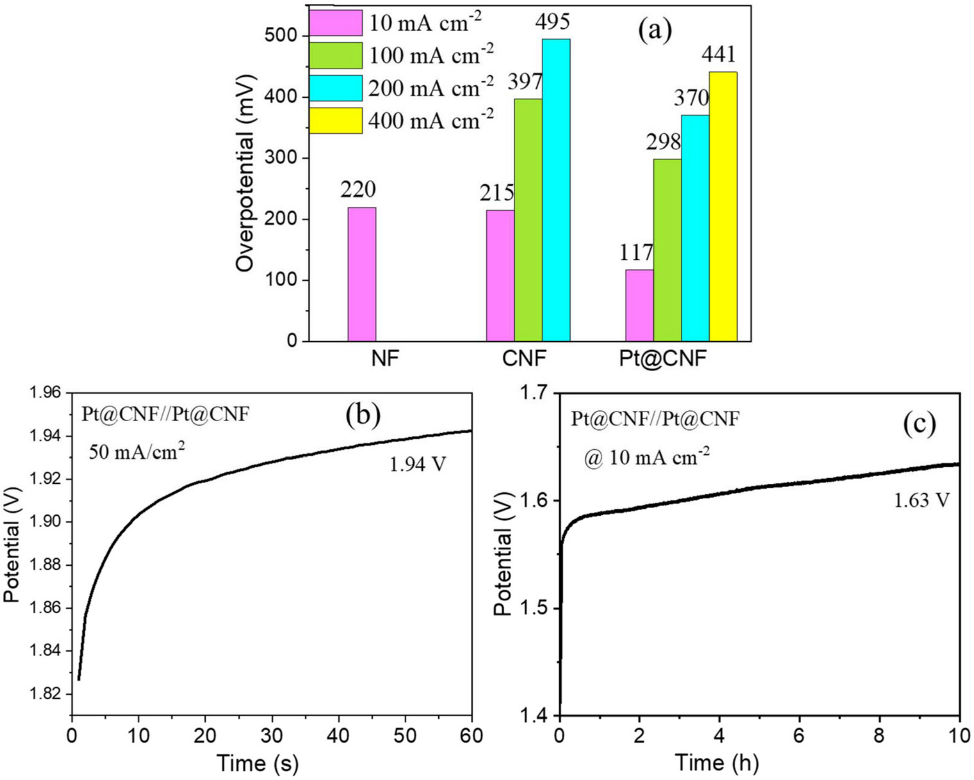

Fig. 8 (a) Overpotential comparison of NF, CNF, and Pt@CNF; (b) chronopotentiometry of Pt@CNF (two electrode system) at 50 mA cm^{-2} for 60 s; and (c) chronopotentiometry of Pt@CNF *vs*. Pt@CNF two electrode system.

unchanged after the HER process, indicating good structural stability of the Pt sites. This is further supported by the Pt 4f XPS spectrum, which shows no significant shift in binding energy, confirming that the chemical state of Pt remains stable post-HER. Additionally, a substantial decrease in the atomic percentage of Fe is observed from 1.2% to 0.6% in Pt@CNF, and from 2.9% to 1.1% in pure CNF. A similar decline in the Co content is also detected, pointing to structural changes or partial dissolution of the active layer under electrochemical conditions. The K insertion from the KOH electrolyte is confirmed from the EDX analysis of both CNF and Pt@CNF.

Conclusion

In summary, Pt@CNF was successfully synthesized *via* a two-step strategy involving electrodeposition of CNF and subsequent chemical reduction of Pt nanoparticles. The incorporation of Pt significantly enhances the HER performance in alkaline media, as evidenced by a low overpotential of 117 mV at 10 mA cm^{-2}, a high theoretical hydrogen yield of 7.7 μmol, and a TOF of 14.6×10^{-3} s^{-1}, which is double that of pristine CNF. These improvements are attributed to the synergistic interactions between Pt and CNF, which enhance the intrinsic activity with an increased electrochemically active surface area and increased number of accessible active catalytic sites. The improved conductivity and reduced solution resistance of Pt@CNF, as evidenced by EIS, further reinforce its superior HER activity. Although a slightly higher Tafel slope is observed for Pt@CNF, this is likely due to changes in RDS and modified reaction kinetics induced by Pt incorporation. The results demonstrate the potential of Pt@CNF as a promising electrocatalyst for efficient HER applications in alkaline media.

Conflicts of interest

There are no conflicts of interest to declare.

Data availability

All data supporting the findings of this study are available within this article and its SI. Supplementary information is available. See DOI: **https://doi.org/10.1039/d5dt01617g**.

Additional data are available from the corresponding author upon reasonable request.

Acknowledgements

The first author thanks the Vellore Institute of Technology (VIT) Chennai, Tamil Nadu, India for a post-doc fellowship.

References

1 J. Hu, C. Zhang, L. Jiang, H. Lin, Y. An, D. Zhou, M. K. Leung and S. Yang, *Joule*, 2017, **1**(2), 383–393.

2 B. Wang, X. Chen, Y. He, Q. Liu, X. Zhang, Z. Luo, J. V. Kennedy, J. Li, D. Qian, J. Liu and G. I. Waterhouse, *Appl. Catal., B*, 2024, **346**, 123741.

3 H. S. Jadhav, A. Roy, B. Z. Desalegan and J. G. Seo, *Sustainable Energy Fuels*, 2020, **4**(1), 312–323.

4 K. M. Naik, E. Higuchi and H. Inoue, *Nanoscale*, 2020, **12**(20), 11055–11062.

5 K. M. Naik, E. Higuchi and H. Inoue, *Int. J. Hydrogen Energy*, 2023, **48**(79), 30741–30750.

6 R. Fan, Q. Mu, Z. Wei, Y. Peng and M. Shen, *J. Mater. Chem. A*, 2020, **8**(19), 9871–9881.

7 K. M. Naik, K. Hashisake, E. Higuchi and H. Inoue, *Mater. Adv.*, 2023, **4**(2), 561–569.

8 K. M. Naik and S. Sampath, *Electrochim. Acta*, 2017, **252**, 408–415.

9 Y. Liu, Q. Wang, J. Zhang, J. Ding, Y. Cheng, T. Wang, J. Li, F. Hu, H. B. Yang and B. Liu, *Adv. Energy Mater.*, 2022, **12**(28), 2200928.

10 P. Stelmachowski, J. Duch, D. Sebastián, M. J. Lázaro and A. Kotarba, *Materials*, 2021, **14**(17), 4984.

11 S. G. Ji, H. Kim, W. H. Lee, H. S. Oh and C. H. Choi, *J. Mater. Chem.*, 2021, **9**(35), 19834–19839.

12 G. Zhao, B. Wang, Q. Yan and X. Xia, *J. Alloys Compd.*, 2022, **902**, 163738.

13 P. Li, X. Hu, Z. Zhang, X. Zhang, N. Zeng, C. Hu, B. Yu, X. Hu, J. Song, Y. Shi and L. Zhou, *Appl. Surf. Sci.*, 2023, **611**, 155780.

14 G. Chen, T. Wang, J. Zhang, P. Liu, H. Sun, X. Zhuang, M. Chen and X. Feng, *Adv. Mater.*, 2018, **30**(10), 1706279.

15 M. Wang, J. Q. Wang, C. Xi, C. Q. Cheng, C. G. Kuai, X. L. Zheng, R. Zhang, Y. M. Xie, C. K. Dong, Y. J. Chen and X. W. Du, *Small*, 2021, **17**(21), 2100203.

16 H. Yu, W. Wang, Q. Mao, K. Deng, Z. Wang, Y. Xu, X. Li, H. Wang and L. Wang, *Appl. Catal., B*, 2023, **330**, 122617.

17 S. W. Jang, S. Dutta, A. Kumar, Y. R. Hong, H. Kang, S. Lee, S. Ryu, W. Choi and I. S. Lee, I.S, *ACS Nano*, 2020, **14**(8), 10578–10588.

18 X. He, X. Han, X. Zhou, J. Chen, J. Wang, Y. Chen, L. Yu, N. Zhang, J. Li, S. Wang and H. Jin, *Appl. Catal., B*, 2023, **331**, 122683.

19 X. Meng, J. Han, L. Lu, G. Qiu, Z. L. Wang and C. Sun, *Small*, 2019, **15**(41), 1902551.

20 B. Wang, Z. Luo, H. Sun, M. Chen, Y. Zhang, X. Zhao, G. Qiu, B. Xiao, T. Zhou, Q. Lu and D. Li, *J. Energy Chem.*, 2025, **107**, 427–439.

21 Y. Feng, R. Ma, M. Wang, J. Wang, T. Sun, L. Hu, J. Zhu, Y. Tang and J. Wang, *Phys. Chem. Lett.*, 2021, **12**(30), 7221–7228.

22 P. Babar, A. Lokhande, V. Karade, B. Pawar, M. G. Gang, S. Pawar and J. H. Kim, *ACS Sustainable Chem. Eng.*, 2019, **7**(11), 10035–10043.

23 S. Anantharaj, S. R. Ede, K. Karthick, S. S. Sankar, K. Sangeetha, P. E. Karthik and S. Kundu, *Energy Environ. Sci.*, 2018, **11**(4), 744–771.

24 H. S. Jadhav, A. Roy, B. Z. Desalegan and J. G. Seo, *Sustainable Energy Fuels*, 2020, **4**(1), 312–323.

25 D. Cheng, Q. Zhong, Y. Xiong, Y. Bu and J. Wang, *J. Alloys Compd.*, 2020, **817**, 152689.

26 Y. Wu, Y. Li, Z. Xie, Y. Wang, Y. Wang and B. Wei, *Chem. Eng. J.*, 2024, **488**, 151086.

27 Z. Zhao, J. Yang, J. Lin, X. Wang, D. Chen, L. Jiao, Q. Zhang, Y. Hou, Z. Ye and J. Lu, *J. Energy Storage*, 2023, **65**, 107360.

28 Y. Yang, Y. Song, S. Mo and M. Liu, *Chem. Eng. J.*, 2021, **417**, 127934.

29 S. Nayak and K. M. Parida, *Sci. Rep.*, 2019, **9**(1), 2458.

30 H. Wang, Q. He, F. Zhan and L. Chen, *J. Colloid Interface Sci.*, 2023, **630**, 286–296.

31 Y. Shi, J. Li, B. Zhang, S. Lv, T. Wang and X. Liu, *Appl. Surf. Sci.*, 2021, **565**, 150506.

32 T. Li, T. Zheng, T. Hui, J. Pan, R. Zhang, H. Liu, Z. Liu, C. Xu and X. Meng, *Appl. Surf. Sci.*, 2024, **668**, 160397.

33 Y. Arafat, Y. Zhong, M. R. Azhar, M. Asif, M. O. Tadé and Z. Shao, *EcoMat*, 2023, **5**(10), e12394.

34 J. Yao, D. Xu, X. Ma, J. Xiao, M. Zhang and H. Gao, *J. Power Sources*, 2022, **524**, 231068.

35 A. Karmakar, B. B. Kamble, R. Madhu, P. Gudlur and S. Kundu, *J. Mater. Chem. A*, 2023, **11**(47), 26023–26043.

36 F. Bao, E. Kemppainen, I. Dorbandt, R. Bors, F. Xi, R. Schlatmann, R. van de Krol and S. Calnan, *ChemElectroChem*, 2021, **8**(1), 195–208.

37 J. Liang, H. Shen, Y. Ma, D. Liu, M. Li, J. Kong, Y. Tang and S. Ding, *Dalton Trans.*, 2020, **49**(32), 11217–11225.

38 G. Rajeshkhanna, T. I. Singh, N. H. Kim and J. H. Lee, *ACS Appl. Mater. Interfaces*, 2018, **10**(49), 42453–42468.

39 D. Liu, J. Liu, B. Xue, J. Zhang, Z. Xu, L. Wang, X. Gao, F. Luo and F. Li, *ChemElectroChem*, 2023, **10**(4), e202201025.

40 S. Anantharaj, K. Karthick, M. Venkatesh, T. V. Simha, A. S. Salunke, L. Ma, H. Liang and S. Kundu, *Nano Energy*, 2017, **39**, 30–43.

41 S. Vijaya and L. J. Kennedy, *J. Electrochem. Soc.*, 2024, **171**(6), 066501.

42 Q. Cai, W. Hong, C. Jian, X. He and W. Liu, *Adv. Energy Sustainability Res.*, 2023, **4**(6), 2200178.

43 Y. C. Zhang, M. Zhao, J. Wu, Y. Wang, L. Zheng, F. Gu, J. J. Zou, J. Gao and X. D. Zhu, *ACS Catal.*, 2024, **14**(10), 7867–7876.

44 N. Dubouis and A. Grimaud, *Chem. Sci.*, 2019, **10**(40), 9165–9181.

45 J. D. Benck, T. R. Hellstern, J. Kibsgaard, P. Chakthranont and T. F. Jaramillo, *ACS Catal.*, 2014, **4**(11), 3957–3971.

46 S. Vijaya and L. J. Kennedy, *Fuel*, 2024, **373**, 132354.

47 S. Anand Kumar and L. John Kennedy, *Int. J. Hydrogen Energy*, 2024, **96**, 1101–1118.

48 X. Yang, S. Li, Y. Zhang, F. Qiu, Y. Sun, W. Ning, Q. Tao, W. Li and S. Miao, *J. Mater. Chem. A*, 2024, **12**(28), 17574–17585.

49 R. Maurya, R. Das, S. Sharma and M. Neergat, *Phys. Chem. Chem. Phys.*, 2024, **26**(13), 10091–10100.

50 L. R. L. Ting, Y. Deng, L. Ma, Y. J. Zhang, A. A. Peterson and B. S. Yeo, *ACS Catal.*, 2016, **6**(2), 861–867.

51 X. D. Wang, H. Y. Chen, Y. F. Xu, J. F. Liao, B. X. Chen, H. S. Rao, D. B. Kuang and C. Y. Su, *J. Mater. Chem. A*, 2017, **5**(15), 7191–7199.

52 X. Yang, J. Cheng, Y. Xu, H. Li, W. Tu and J. Zhou, *Chem. Eng. J.*, 2023, **472**, 145076.

53 D. Delgado, M. Minakshi and D. J. Kim, *Int. J. Electrochem. Sci.*, 2015, **10**(11), 9379–9394.

54 Y. Zheng, R. Gao, Y. Qiu, L. Zheng, Z. Hu and X. Liu, *Inorg. Chem.*, 2021, **60**(7), 5252–5263.

55 C. Song, Y. Liu, Y. Wang, S. Tang, W. Li, Q. Li, Q. J. Zeng, L. Chen, H. Peng and Y. Lei, *Sci. China Mater.*, 2021, **64**(7), 1662–1670.